# Composite Thermal Conductivity in a Large Heterogeneous Porous Methane Hydrate Sample

**6 AUTHORS**, INCLUDING:

Timothy J. Kneafsey

Lawrence Berkeley National Laboratory

**102** PUBLICATIONS   **916** CITATIONS

SEE PROFILE

George J. Moridis

Lawrence Berkeley National Laboratory

**232** PUBLICATIONS   **2,524** CITATIONS

SEE PROFILE

M. B. Kowalsky

Lawrence Berkeley National Laboratory

**72** PUBLICATIONS   **1,116** CITATIONS

SEE PROFILE

# Composite Thermal Conductivity in a Large Heterogeneous Porous Methane Hydrate Sample

**Arvind Gupta,[†] Timothy J. Kneafsey,[‡] George J. Moridis,[‡] Yongkoo Seol,[‡] Michael B. Kowalsky,[‡] and E. D. Sloan, Jr.*,[†]**

*Center for Hydrate Research, Chemical Engineering Department, Colorado School of Mines, Golden, Colorado 80401, and Earth Sciences Division, Lawrence Berkeley National Laboratory, Berkeley, California 94720*

By employing inverse modeling to analyze the laboratory data, we determined the composite thermal conductivity ($k_\theta$, W/m/K) of a porous methane hydrate sample ranged between 0.25 and 0.58 W/m/K as a function of density. The calculated composite thermal diffusivities of porous hydrate sample ranged between $2.59 \times 10^{-7}$ m$^2$/s and $3.71 \times 10^{-7}$ m$^2$/s. The laboratory study involved a large heterogeneous sample (composed of hydrate, water, and methane gas). The measurements were conducted isobarically at 4.98 MPa over a temperature range of 277.3−279.1 K. Pressure and temperature were monitored at multiple locations in the sample. X-ray computed tomography (CT) was used to visualize and quantify the density changes that occurred during hydrate formation from granular ice. CT images showed that methane hydrate formed from granular ice was heterogeneous and provided an estimate of the sample density variation in the radial direction. This facilitated quantifying the density effect on composite thermal conductivity. This study showed that the sample heterogeneity should be considered in thermal conductivity measurements of hydrate systems. Mixing models (i.e., arithmetic, harmonic, geometric mean, and square root models) were compared to the estimated composite thermal conductivity determined by inverse modeling. The results of the arithmetic mean model showed the best agreement with the estimated composite thermal conductivity.

## 1. Introduction

Natural gas clathrate hydrates are a class of inclusion compounds formed from a network of water molecules that encapsulate small gas molecules.[1] In general, hydrates form at high pressures and low temperatures in the presence of water and a hydrate-former molecule (i.e., methane, ethane). Worldwide, more than 70 locations of gas hydrate deposits in sediments have been identified based on geophysical, geochemical, and geologic evidence.[2] Gas hydrate deposits are estimated to contain significant amounts of hydrocarbons (mainly methane) on the order of $1-5 \times 10^{15}$ m$^3$ at STP. Therefore, these deposits present a potentially important future energy resource.[3] Recovery of even a fraction of the estimated hydrocarbons contained within the hydrates would provide a substantial alternative energy resource. Gas hydrates are also important in the oil and gas industries because hydrate plugs, which can form pipeline blockages, are of major concern to the flow-assurance community.[1]

Gas hydrates are often referred to as "ice-like" substances due to the similar hydrogen bonding characteristics of the water molecules in ice. However, despite the close structural similarities, the mechanical and thermal properties of hydrates differ from ice. Durham et al.[4] showed that methane hydrate at a given strain rate is over 20 times stronger than ice under similar conditions. The thermal conductivity of hydrate is about one-fifth that of ice.[5−7] Tse et al.[8] used molecular dynamics to show

that the resonant coupling between the guest and the host water molecules was responsible for the low hydrate thermal conductivity, with phonons of heat scattered by the vibrational motions of the guest molecules inside the water cavities.

Hydrate thermal properties play an important role in assessing gas production from natural deposits, sea floor stability of hydrate-bearing oceanic sediments, global climate change, submarine slide formation, and hydrate plug dissociation in oil and gas pipelines.[9,10] Thus, thermal property measurements are crucial in quantifying the role of gas hydrates in these applications. Despite the importance of hydrate thermal properties, few measurements of the methane hydrate thermal conductivity are available in the literature.[7,11−13]

Stern et al.[14] suggested that accurate sample characterization is critical to understanding the hydrate growth, formation, and dissociation processes, as well as to reliably interpreting physical property measurements. Recently, Moridis et al.[15] used X-ray computed tomography (CT) data, as well as pressure and thermal response data coupled with inverse-modeling, to determine the composite thermal conductivity ($k_\theta$, W/m/K) of hydrate-bearing sediments. In this paper, we employ a similar technique to estimate the $k_\theta$ of a porous sample of methane hydrate (without sediment). We used X-ray CT to visualize and quantify the physical state of the sample (i.e., the distribution of the unreacted water and the density changes that occurred during the hydrate formation). This paper presents a new technique to estimate the $k_\theta$ of porous hydrate samples and demonstrates the importance of sample characterization in hydrate physical and thermal property measurements.

* Corresponding author. E-mail: esloan@mines.edu. Telephone: (303)-273-3723. Fax: (303)273-3730.
† Center for Hydrate Research, Chemical Engineering Department, Colorado School of Mines.
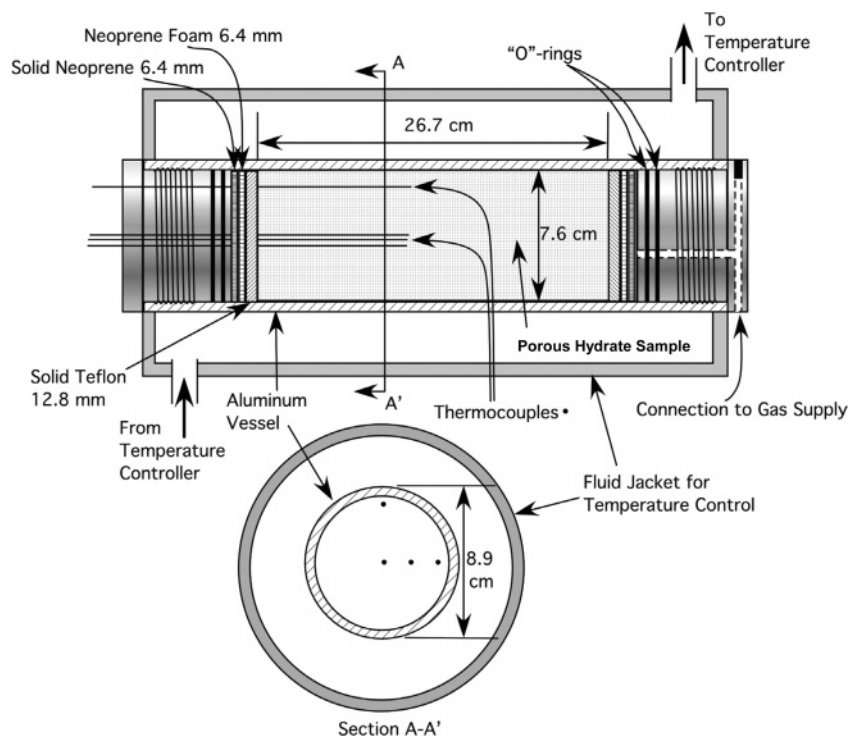‡ Earth Sciences Division, Lawrence Berkeley National Laboratory.

**Figure 1.** Schematic diagram of the pressure vessel. The four dots in Section A−A′ show the nominal locations of the four thermocouples inserted in the vessel.

## 2. Experiment Setup

The experiment was performed in a 7.6 cm i.d. × 26.7 cm long cylindrical aluminum vessel that is transparent to X-rays (Figure 1). The same experimental setup was used to study the hydrate formation and dissociation processes in sediments.[16] Vessel temperature was controlled by circulating a water/glycol coolant solution through the PVC jacket surrounding the vessel. A temperature controller was used to maintain the coolant temperature to within ±0.2 K. Pressure was measured within ±0.007 MPa on the gas inlet line using a Rosemount 1151 pressure transducer. Three type-T thermocouples (45.7 cm long, 0.16 cm diameter, Omega Engineering, Stamford, CT) were used to measure the hydrate sample thermal response. A fourth thermocouple was placed in the vertical direction aligned with the vessel center. For modeling purposes, the exact position of each thermocouple with respect to the vessel center was determined from the CT images.

**2.1. X-ray Computed Tomography.** X-ray computed tomography is a nondestructive and noninvasive technique to visualize hydrate formation and dissociation, providing good spatial and time resolution during these processes.[17−20] In this work, we used a modified Siemens Somatom HiQ medical CT scanner with a peak X-ray beam energy of 133 keV and a current of 120 mA to collect the hydrate sample images. By calibrating the CT scanner using materials of known density, such as water, air, and aluminum, the X-ray attenuation was converted into density. The CT images provide a measure of material density within a specific volume of 250 $\mu$m × 250 $\mu$m × 5 mm (voxel). In our study, axial cross sections of 5 mm thick slices were obtained along the entire sample length, for a total of 54 images with a time resolution of about 2 min.

**2.2. Hydrate Formation.** Methane hydrate was formed in the vessel from 250−850 $\mu$m granular ice particles, using a method similar to that of Stern and co-workers.[21] The ice was packed in layers using a solid cylindrical rod. The objective was to obtain a uniform and compact ice mass in the vessel,

and the layers produced by packing were not visible in the initial CT scan. During the ice packing, the pressure vessel and compacting rod temperatures were maintained below the ice point to avoid ice melting. The initial porosity of the sample (defined as the volume ratio of pore space filled with gas to the total vessel volume) was estimated to be 32%. After packing, the pressure vessel was transferred to the CT table, and the fluid jacket was connected to the coolant line carrying fluid at 265 K.

Methane hydrate was formed by slowly pressurizing (to avoid the ice melting as a result of gas compression) the vessel to 6.2 MPa with 99.9% pure methane gas at 265 K. Figure 2 shows the decrease in pressure with time as methane gas was consumed during the conversion of ice into methane hydrate. Figure 2 also shows the temperature profiles at the measured locations during hydrate formation in the closed system. The bath temperature was raised stepwise to the ice point to enhance the hydrate formation by melting the ice.[21] At about 40 h, we observed a sharp increase in temperature inside the vessel to 277 K (even though the bath temperature was set at 274 K) because of the rapid conversion of melted ice into hydrate. This increase in temperature inside the vessel resulted from the exothermic nature of hydrate formation, and the heat produced was dissipated into the cooler temperature bath (i.e. near the vessel walls) compared to the center of the sample. On the basis of gas consumption and assuming a hydrate stoichiometry of $CH_4 \cdot 6H_2O$,[22] 91 ± 2% (by mass) of the ice was converted into hydrate over 2 days. The final product was a porous sample composed of a matrix of solid methane hydrate, with pores filled with water and methane gas.

CT scans of the entire vessel were recorded at various times (at 0, 27, 42, and 50 h) throughout the hydrate formation process. Figure 3 shows representative CT scans taken at four different locations along the vessel length to illustrate the changes that occurred during the hydrate formation process. These four locations were 60, 120, 180, and 240 mm from one end. These
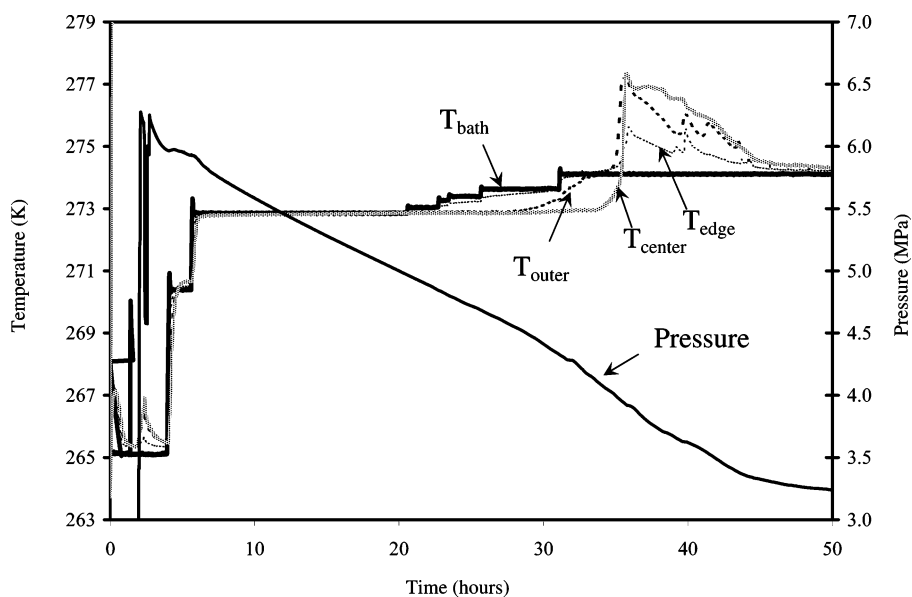
**Figure 2.** Pressure and temperatures during hydrate formation.
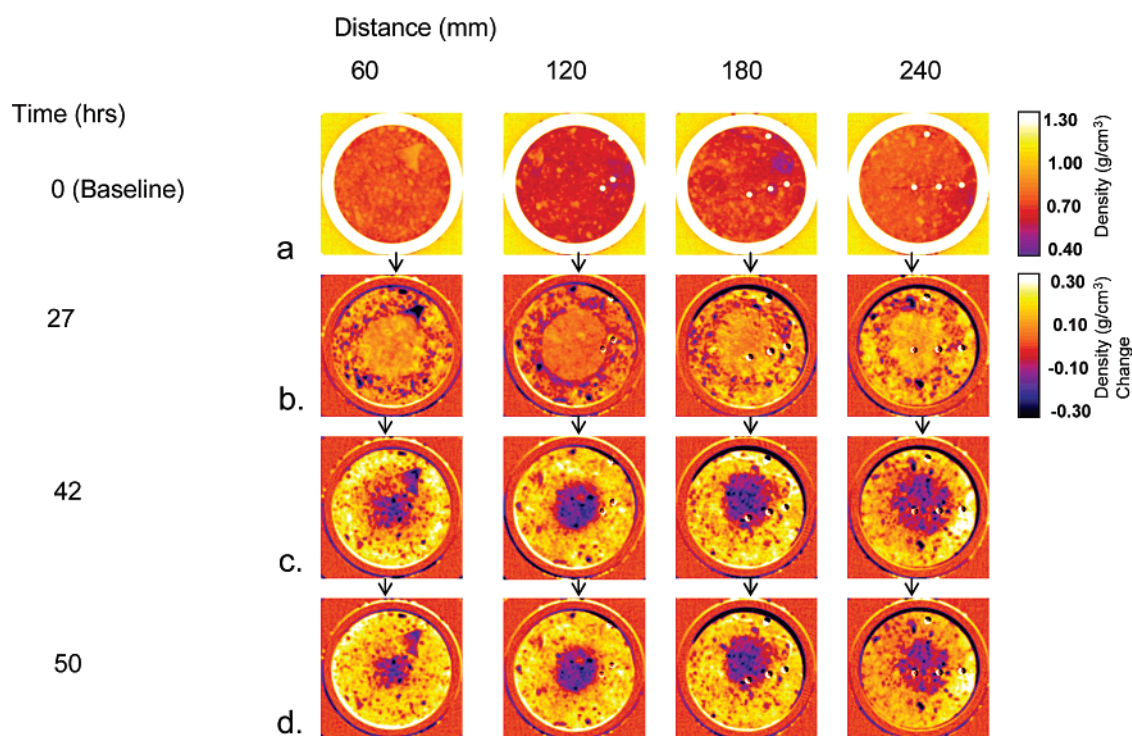


**Figure 3.** CT images at four different locations (60, 120, 180, and 240 mm from one end) during hydrate formation. (a) The baseline images show the porous ice density. The white circle is the aluminum pressure vessel, and the four white interior spots show the thermocouples inserted in the vessel. (b, c, and d) Density changes during hydrate formation. Density increases are yellow and decreases are blue.

four locations show how the sample morphology changed throughout the entire vessel.

Initially ($t = 0$ h), CT scans of the ice-packed vessel showed the presence of some large ice particles in the baseline images (a) taken at 60 and 120 mm, even though we attempted to pack the vessel with uniformly sized ice particles. The presence of large ice particles can be attributed to the ice annealing and particle recrystallization following sieving. Density differences between the initial sample and different stages during hydrate formation were determined by subtracting calibrated density values (Figure 3). At 27 h, we observed a low-density ring (dark) between the vessel and ice along the top throughout the vessel. After 27 h, the temperature was increased above the ice point, and the formation of a less-dense zone (dark area) was observed

at the mid-center zone, whereas the density increased in the outer regions close to the vessel boundary (at 42 and 50 h).

Kneafsey et al.[16] suggested that changes in sample densities for a water, gas, hydrate, and silica sand system can be caused by four processes: hydrate formation, water saturation changes, mechanical changes, and gas pressure changes. The corresponding sensitivity analysis showed that the change in water saturation caused the largest density variation. In our study, X-ray CT images showed that the hydrate did not form uniformly across the radius of the sample and formed more efficiently at the outer zone of the sample as compared to the center. We believe the presence of the low-density zone in the sample center is caused by water movement away from the center in the radial direction during rapid hydrate formation
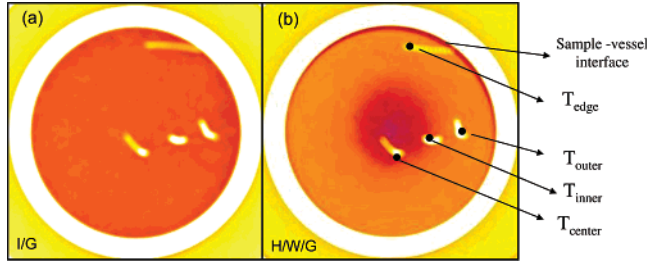
**Figure 4.** Average X-ray CT images of 51 (out of 54) cross sections, before (left) and after hydrate formation (right). The outer white circle is the aluminum pressure vessel. The four white interior spots are the thermocouples, and interior black spots (right) indicate the end of thermocouples. The low-density zone close to the sample−vessel interface formed during hydrate formation.

above the ice point, starting at about 40 h. Hydrate formation can reduce the pore capillary pressure and cause migration of the aqueous phase toward the formation zone. A similar observation was reported by Kneafsey et al.[16] for a sand/hydrate/water/gas system during the hydrate formation process. Dorstewitz and Mewes[23] studied the hydrate formation mechanism in gas pipelines and observed that the capillary effects caused water to move toward the hydrate formation zone.

**2.3. Thermal Tests.** The temperature response of the sample was measured over time using the thermocouples denoted as $T_{outer}$, $T_{inner}$, and $T_{center}$ in Figure 4. We conducted two thermal tests at pressure and temperature conditions within the methane hydrate stability zone. The equilibrium temperature of methane hydrate is 279.6 K at 4.98 MPa.[24] The first thermal test involved a near-step decrease of the bath temperature from 279.1 to 277.3 K at a constant pressure of 4.98 MPa. In the second thermal test, the bath temperature was increased from 277.3 to 279.1 K at 4.98 MPa. Temperature data were collected every 20 s using a Keithley 2750 data acquisition system. In both tests, pressure was also continuously monitored and kept constant by connecting to a large methane gas cylinder.

## 3. Determination of Sample Composite Density and Specific Heat

Figure 4 shows the axially averaged sample CT images before and after hydrate formation. Thus, Figure 4a shows granular ice and methane gas, and Figure 4b shows methane hydrate, free methane gas, and water. We employed the image processing program ImageJ[25] to convert X-ray attenuation distributions to composite density ($\rho_\theta$), using a calibration curve determined from X-ray attenuation and material density. Figure 5 shows the variation of composite density, $\rho_\theta$ in the radial direction before and after hydrate formation. The composite density of porous ice was determined from the CT image (averaging the density along the entire radial direction from 0 to 3.8 cm at $t = 0$ h) to be about 643 kg/m³, which is within 1% of the composite density determined from the estimated initial porosity, $\varphi$, of 32% (see Section 2.2), and the densities of ice (I), $\rho_I$, and methane gas (G), $\rho_G$, at 6.2 MPa and 265 K (see Table 1):

$$\rho_\theta = \rho_I(1 - \varphi) + \rho_G \varphi \tag{1}$$

The good agreement between the measured and the calculated composite density for porous ice validates our approach of estimating sample density using CT images and also illustrates the utility of this technique.

Figure 5 shows that after formation of the hydrate (at $t = 50$ h), the composite sample density ranged from 420 kg/m³ (center, zone 1) to 727 kg/m³ (edge, zone 3). This was in contrast to

the porous ice, which had a far more uniform composite density, fluctuating between 600 and 700 kg/m³ in the radial direction. On the basis of the significant density variation after hydrate formation, the sample was divided into three different zones: the low-density center ($\rho_{av} = 420$ kg/m³, zone 1), the transition zone ($\rho_{av} = 545$ kg/m³, zone 2), and the high-density outer zone ($\rho_{av} = 727$ kg/m³, zone 3). The density variation results from the variation in the phase saturations (S) of hydrate, water, and gas in the radial direction. There is no ice present in the system because system temperature is well above the ice point.

As shown in eq 2a, the composite density reflects the combined contributions of the hydrate (H), water (W), and gas phases. Because we have three unknowns in each zone ($S_H$, $S_G$, and $S_w$) and two independent relationships (eqs 2b and 3), it is not possible to determine the unique phase saturation values of hydrate, water, and gas phases in each zone. Therefore, we obtained the range of phase saturations that satisfies eqs 2b and 3, using the simple iterative procedure described below.

$$\rho_\theta = \rho_G S_G + \rho_H S_H + \rho_W S \tag{2a}$$

where for each zone (z) of volume $V_z$ (m³),

$$S_H = \frac{V_H}{V_z}; \qquad S_G = \frac{V_G}{V_z}; \qquad S_W = \frac{V_W}{V_z}$$

$$\rho_\theta = \rho_G S_G + \rho_H S_H + \rho_W(1 - S_H - S_G) \tag{2b}$$

$$S_G + S_H + S_W = 1 \tag{3}$$

There are only small ranges of $S_H$, $S_G$, and $S_W$ values that can satisfy eqs 2b and 3 and also give physically realistic values (i.e., $S_H$, $S_G$, and $S_W$ can only take values between 0 and 1). From eqs 2a and 3, eq 2a can be rewritten in the form of eq 2b. To estimate phase saturations, an initial guess value for $S_G$ is input into eq 2b, and density values of pure water, gas, and hydrate are obtained from Table 1. Using the value of $\rho_{\theta,zone1} = 420$ kg/m³ determined from the CT images in zone 1, a value of $S_H$ can then be calculated. If the value of $S_H$ is between 0 and 1 and eq 3 is satisfied, the $S_H$ value is accepted. Otherwise it is rejected. This procedure is repeated for different guess value of $S_G$ such that a range of acceptable $S_H$, $S_G$, and $S_W$ are calculated for zone 1. Using this simple procedure, we calculated saturations of between $0.562 < S_{G,zone1} < 0.602$, $0.006 < S_{H,zone1} < 0.434$, and $0.004 < S_{W,zone1} < 0.392$ for zone 1. Applying this same procedure to zones 2 and 3, ranges of $S_G$, $S_H$, and $S_W$ were calculated using the composite density determined from CT images in zones 2 and 3, respectively. The calculated saturations of between $0.419 < S_{G,zone2} < 0.472$, $0.007 < S_{H,zone2} < 0.574$, and $0.007 < S_{W,zone2} < 0.512$ for zone 2, and $0.210 < S_{G,zone3} < 0.283$, $0.006 < S_{H,zone3} < 0.787$, and $0.003 < S_{W,zone3} < 0.711$ for zone 3.

Finally, to ensure the mass balance of all phases was satisfied, we determined the combinations of phase saturations of hydrate, water, and gas in each zone. The phase saturations combinations were determined by minimizing the difference between the corresponding estimated and measured mass of each phase, using the following general equation:

$$\rho_x(V_{zone1} S_{x,zone1} + V_{zone2} S_{x,zone2} + V_{zone3} S_{x,zone3}) = m_{x,estim} \tag{4}$$

where x = H, G, W (mass fraction).

The mass of hydrate formed ($m_{H,meas}$) was determined from the gas consumption measurements by assuming hydration number equal to 6 and the initial mass of ice added to the vessel.
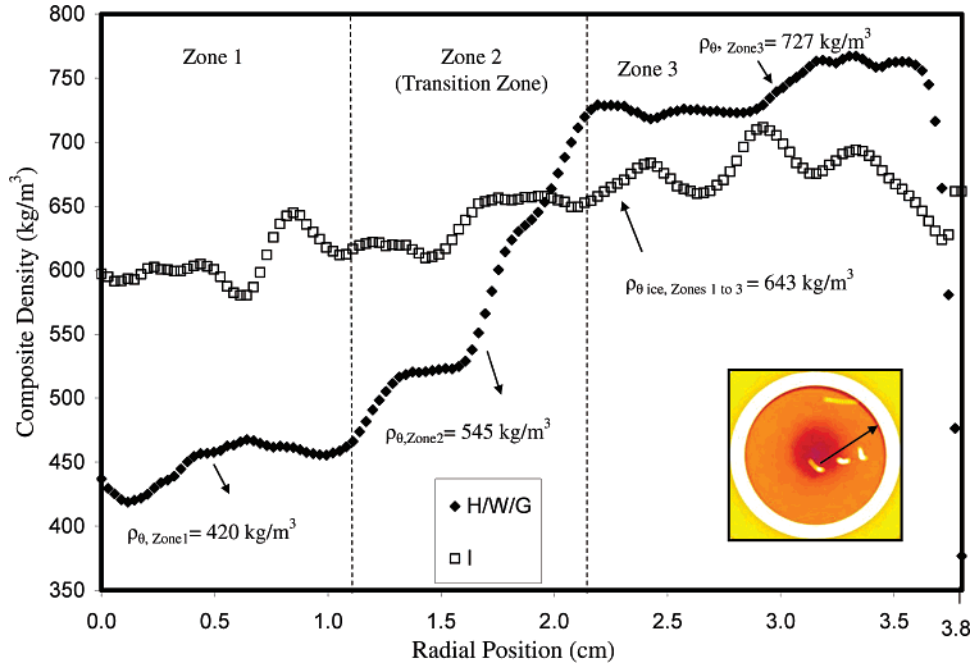
**Figure 5.** Measured composite density in the radial direction. The porous ice density was averaged along the arrow shown in the CT image. The sample composite density changed in the radial direction after hydrate formation. Based on the density variation, the core was divided into three different regions, zones 1, 2, and 3.

**TABLE 1: Phase Properties**[a]

| phase | $C$ (J/kg/K) | $\rho$ (kg/m³) | $k$ (W/m/K) |
|---|---|---|---|
| ice | 2040 | 917 | 2.23 |
| hydrate | 2080 | 910 | 0.575 |
| water (at 4.98 MPa, 277 K) | 4188 | 1000 | 0.57 |
| methane gas (at 4.98 MPa, 277 K) | 2612 | 38.9 | 0.035 |

Both water and gas properties were calculated using National Institute of Standards and Technology (NIST) Program.[26,32] Pure ice and methane hydrate properties were obtained from Sloan.[1] Methane hydrate thermal conductivity was taken from Huang and Fan.[6]

In this way, the percentage of the ice conversion to hydrate was obtained, thereby giving the mass of hydrate produced and the mass of unreacted water (the experiment was performed above the ice point) in the system. The mass of gas was also calculated using the methane gas density[26] multiplied by the available pore volume. The pore volume was calculated by subtracting the volume of hydrate and water phases from the total vessel volume. $V_{zone1}$, $V_{zone2}$, and $V_{zone3}$ were determined from the radial distance of each zone (determined from the CT images) and the vessel geometry.

Guess values of $S_{H,zone1}$, $S_{H,zone2}$, and $S_{H,zone3}$ (within the saturation range determined from eqs 2 and 3) were entered into eq 4 for x = H, and the mass of hydrate ($m_{H,estim}$) was then calculated. Using a conjugate solver, the value of $m_{H,estim}$ was compared with $m_{H,meas}$, and the values of $S_{H,zone1}$, $S_{H,zone2}$, and $S_{H,zone3}$ were adjusted until $m_{H,estim}$ was in very good agreement with $m_{H,meas}$. The solver simultaneously adjusted the values of $S_{G,zone1}$, $S_{G,zone2}$, and $S_{G,zone3}$ and $S_{W,zone1}$, $S_{W,zone2}$, and $S_{W,zone3}$ in zones 1−3 by matching the estimated and measured mass of gas and water phases using eq 4 for x = G, W. Finally, this results in upper and lower limits values of hydrate, gas, and water saturations in zones 1−3.

After determining the combinations of saturations in zones 1, 2, and 3, we computed the range of composite-specific heats ($C_\theta$, J/kg/K) from:

$$C_\theta = C_W X_W + C_H X_H + C_G X_G \tag{5}$$

where

$$X_i = \frac{m_{i,zone1}}{(m_{W,zone1} + m_{G,zone1} + m_{H,zone1})};$$

$$m_{i,zone1} = (\rho_i \times V_{zone} \times S_{i,zone1})$$

Therefore, from the combinations of saturation values determined above, $m_{i,zone1}$, $m_{i,zone2}$, and $m_{i,zone3}$ are easily calculated. Using values of $C_W$, $C_H$, and $C_G$ (Table 1), the composite specific heats of zones 1−3 were determined. The estimated range of specific heat values in each zone was used in the inverse modeling simulations to estimate the sample composite thermal conductivity.

## 4. Inverse Modeling Using ITOUGH2

In this study, we determined the composite thermal conductivity of a porous methane hydrate sample (consisting of hydrate, water, and gas) by a history-matching technique using ITOUGH2.[27] ITOUGH2 uses an optimization approach for parameter estimation in problems involving nonisothermal multiphase flow in porous media; it has been validated against many field and laboratory data sets.[28−31] ITOUGH2 is capable of handing nonreactive phases, and in this case, hydrate does not pose any problems because both tests were performed under thermodynamically stable hydrate conditions.

**4.1. Composite Thermal Conductivity Estimation and Validation.** The cylindrical hydrate sample was assumed to be axially symmetric and was modeled as a one-dimensional radial system. The domain, consisting of the composite hydrate sample (containing hydrate, water, and methane gas) was divided into 380 gridblocks of uniform $\Delta r = 10^{-4}$ m. Owing to heterogeneity in the radial direction, we divided the hydrate sample into three different zones. The exact length of each zone and location of each thermocouple were determined from the CT images. This information was used to assign the thermal data in the radial direction in the simulations.

The CT image in Figure 4b shows the presence of a gas gap between the sample and the aluminum vessel wall. This gap
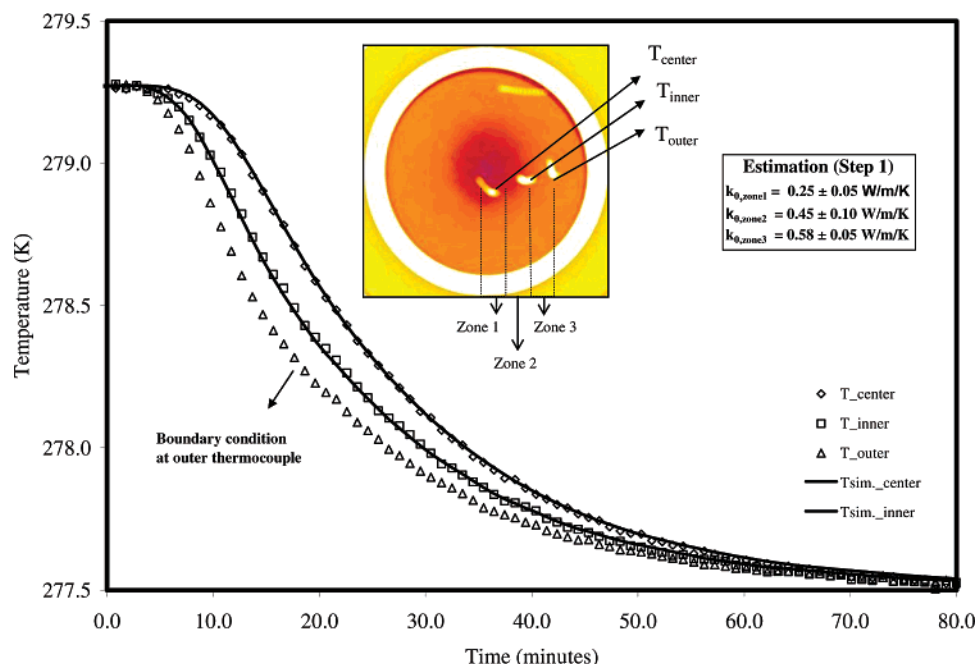
**Figure 6.** Calibration and parameter determination from cooling data in the H/W/G system by inverse modeling. Each zone optimum composite thermal conductivity ($k_\theta$) was estimated by minimizing the difference between computed and measured thermal data. The symbols represent data, and lines represent model results.

width is nonuniform, which may result in a nonuniform radial heat flux between the sample and the bath. To address this problem, we used the thermocouple at the outer thermocouple as the outer boundary (instead of the thermocouple in the bath) in the simulation.

For the radial heat conduction process, the rate of heat flow is dictated by the medium's thermal diffusivity (m$^2$/s) [($\alpha_\theta = k_\theta/(\rho_\theta \times C_\theta)$]. Because of nonflowing conditions, we assume no advective flow, and consequently, heat transfer occurs only through conduction. Within a zone, gridblocks were assigned a uniform value of composite density and specific heat. Subsequently, we estimated the composite thermal conductivity ($k_\theta$) of each zone by minimizing the differences between the observed and predicted thermal response using history matching. The optimal $k_\theta$ values in zones 1−3 were determined using the following procedure. An initial guess value of $k_\theta$ was used to calculate the thermal diffusivity in each zone. From Fourier's equation of conduction, the thermal response of different zones in the sample could be predicted from the thermal diffusivity. The $k_\theta$ guess value was then adjusted until the observed and predicted thermal responses were in agreement.

The thermal conductivity estimation process involved two steps. In step 1, individual zone composite thermal conductivities ($k_\theta$) were optimized and estimated by inverse modeling of the first thermal data set (temperature decrease) using ITOUGH2 (as described above). In the inverse modeling, we used the conditions at the outer thermocouple as a boundary and predicted the temperature response of the two internal thermocouples.

Figure 6 shows the comparison between observed and predicted temperature versus time profiles during the first thermal test (decreasing the temperature from 279.1 to 277.3 K), for the optimal values of $k_{\theta,zone1}$, $k_{\theta,zone2}$, and $k_{\theta,zone3}$, equal to 0.25, 0.45, and 0.58 W/m/K, respectively. These optimized values of composite thermal conductivity were consistent within ±0.05 W/m/K for zones 1 and 3 and ±0.10 W/m/K for zone 2. In contrast to zones 1 and 3, the composite thermal conductivity of zone 2 (transition region) exhibited a larger error in the estimation. This was attributed to the variation in the bulk density determined from the CT images (see Figure 5).

In step 2, we assigned the estimated composite thermal conductivities ($k_\theta$) to each zone and performed the forward simulation to predict the thermal response at the internal thermocouple locations for the temperature increase at the outer thermocouple (277.3−279.1 K). Figure 7 shows the comparison between the observed and predicted temperature versus time profiles for the heating test. The proximity between observed and predicted profiles validated the estimated $k_\theta$ for each zone that was derived in step 1. The dotted lines in Figure 7 show the simulation results corresponding to the 25% lower values than the estimated thermal conductivities of each zone. For the center thermocouple, this is not the best fit curve. However for the inner thermocouple in zone 2, both curves appear to fit the data relatively well. This result is consistent with the large error associated with the $k_\theta$ for zone 2.

Using the same two-step thermal conductivity estimation process (estimation and validation), we also estimated the volume-averaged thermal conductivity for the hydrate sample by matching the thermal data. The estimated optimal value of volume-averaged thermal conductivity, $k_\theta$, was 0.49 ± 0.05 W/m/K, corresponding to the averaged $\rho_\theta$ and $C_\theta$ equal to 550 kg/m$^3$ and 2449 J/kg/K, respectively. Because we used the outer thermocouple as a boundary, the volume-averaged density and heat capacity were calculated only up to the radial position of outer thermocouple instead of the complete sample. This estimated volume-averaged composite thermal conductivity would be equivalent to simulations made without the CT scanning data.

The inverse modeling simulations were performed for the entire range of phase saturations determined in Section 3 and yielded the optimal values of composite thermal conductivity ($k_\theta$). For some saturation values, unrealistic thermal conductivities values were obtained, e.g., an estimated thermal conductivity in zone 2 was higher than that in zone 3, despite its lower density. Such cases were omitted from the final results.

## 5. Comparison with Mixing Models

Our inverse modeling results showed that the sample composite thermal conductivity ($k_\theta$) ranged between 0.25 and 0.58
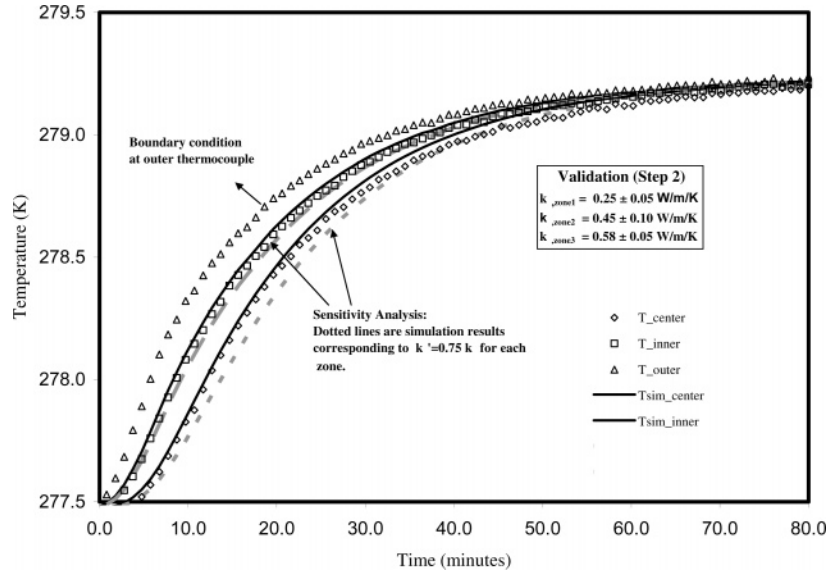
**Figure 7.** Prediction of heating test response and validation of the parameters ($k_{\theta,\text{zone}1}$, $k_{\theta,\text{zone}2}$, and $k_{\theta,\text{zone}3}$) determined in step 1. The symbols represent data, and lines represent model results.
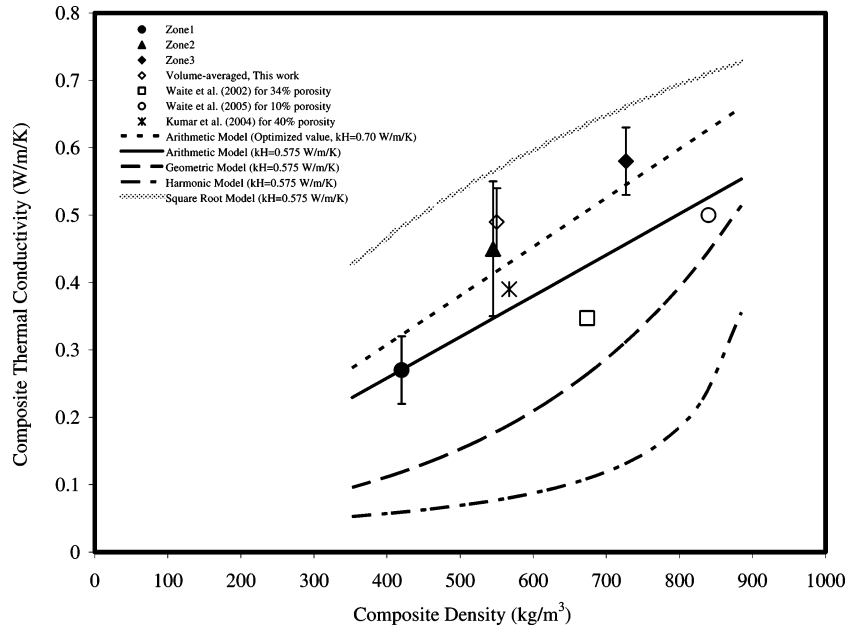


**Figure 8.** Comparison between estimated composite thermal conductivity, literature values, and predictions of mixing models (on values given in Table 1).

W/m/K (zones 1−3). As a further test of the $k_\theta$ values obtained from the inverse modeling, we compared the mixing models to independently predict the $k_\theta$ as a function of phase saturation. Equations 6−9 show the arithmetic, harmonic, geometric, and square root mean models, respectively:

$$k_\theta = k_H S_H + k_W S_W + k_G S_G \tag{6}$$

$$k_\theta = \left( \frac{S_H}{k_H} + \frac{S_W}{k_W} + \frac{S_G}{k_G} \right)^{-1} \tag{7}$$

$$k_\theta = k_H S_H \times k_W S_W \times k_G S_G \tag{8}$$

$$k_\theta = k_H \sqrt{S_H} + k_w \sqrt{S_w} + k_G \sqrt{S_G} \tag{9}$$

Note that, to predict the composite thermal conductivity in these mixing models, the pure methane hydrate thermal conductivity ($k_H$) with zero porosity is needed. However, no such data are available in the literature because of the

experimental difficulties involved in synthesizing a nonporous methane hydrate sample. Using water and gas thermal conductivity values from Table 1[32] and assuming $k_H = 0.575$ W/m/K,[6] we calculated the $k_\theta$ for each zone based on $S_H$, $S_G$, and $S_W$ determined in Section 3.

In Figure 8, we plot the $k_\theta$ values for each zone obtained from inverse modeling, the literature, and the mixing models as a function of sample density.[5,33,34] As expected, the composite thermal conductivity increases with density. Figure 8 also shows that our estimates of $k_\theta$ are higher than those obtained from the mixing models except the square root mean model. The arithmetic mean model predictions are closer to our estimated values than the harmonic, geometric, and square root mean models. Because the arithmetic model predictions are closest to our estimated $k_\theta$ values, we used this model to predict the zero-porosity methane hydrate thermal conductivity by imputing our estimated $k_\theta$ into the arithmetic model using inverse modeling. Using eq 6, an optimized value of $k_H = 0.70 \pm 0.04$
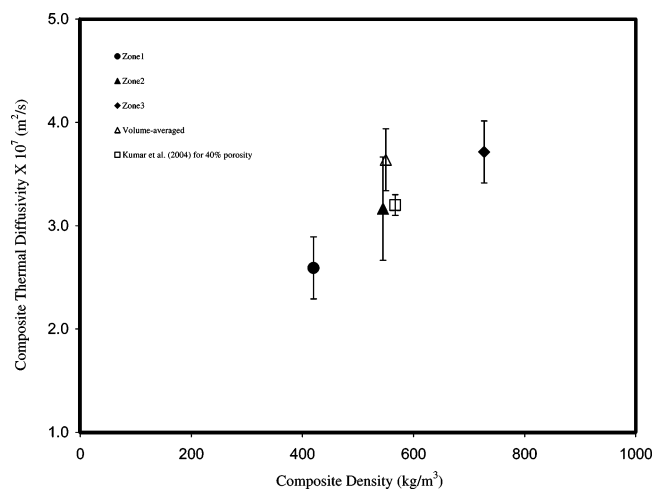
**Figure 9.** Comparison between estimated composite thermal diffusivity and literature value.

W/m/K would be required to match within error bars of the estimated composite thermal conductivities. The predicted value is approximately 28.6% higher than the value reported by Huang et al.[6]

Our $k_\theta$ estimates are higher than the values reported in the literature for the same density.[5,11,12,33] This difference can be attributed to the presence of unreacted water in our hydrate sample, compared to the porous methane hydrate samples (with the pore space filled only with gas) used in all the reported measurements. Because of the hydrophilic nature of the hydrate particles,[35] liquid water will adsorb onto the hydrate surface, and capillary-held water can provide a thermal bridge between the hydrate particles. This facilitates effective heat transfer and results in a higher effective thermal conductivity of the medium.

Recently, Huang and Fan reported that the thermal conductivity of the methane hydrate formed from SDS solution increased from 0.33 to 0.57 W/m/K with 2 MPa impaction in the axial direction.[6] Because of the lack of their hydrate sample porosity and density data information, we could not plot their data in Figure 8. Figure 8 also shows that the estimated volume-averaged thermal conductivity is in good agreement with the arithmetic model prediction of composite thermal conductivity with density. This result suggests that the volume-averaged properties adequately describe the heat transfer in this study. On the local scale, however, heat transfer would be overpredicted in one region and underpredicted in another. Knowledge of the sample heterogeneity allowed us to correctly attribute processes and parameters to the location that they occurred rather than the bulk.

In Figure 9, we plot the calculated methane hydrate composite thermal diffusivity, $\alpha_\theta$, with density. The $\alpha_\theta$ increased from $2.59 \pm 0.3 \times 10^{-7}$ m²/s to $3.71 \pm 0.3 \times 10^{-7}$ m²/s from the center to the edge of the sample. The calculated composite thermal diffusivity data is in good agreement with the literature value reported at 281.7 K and 6.79 MPa.[30]

## 6. Conclusions

X-ray CT imaging, used to visualize the heterogeneous porous methane hydrate sample, allowed explicit consideration of the sample heterogeneity. CT images showed that the hydrate sample formed from granular ice was heterogeneous, and the composite density increased from 420 to 727 kg/m³ from the center to the edge of the sample core. This density variation is attributed to the aqueous-phase movement away from the center during the hydrate formation process. This result clearly demonstrates the importance of the X-ray CT imaging technique in hydrate experiments because, in the absence of CT data, the sample would have been assumed to be homogeneous. Furthermore, the spatial heterogeneity in the hydrate sample suggests that the caution should be taken in interpreting hydrate-related processes because the CT images showed that the hydrate can form nonuniformly throughout a sample. This would result in possible misinterpretation of some physical properties measurements such as acoustic wave speed and relative permeability, which are measured along the central axis of a sample, and the results will be attributed to higher hydrate saturation than actually exists in the measurement zone.

In this study, we used an inverse-modeling technique to estimate the composite thermal conductivity of the porous hydrate sample as a function of density. The estimated $k_\theta$ ranged from 0.25 to 0.58 W/m/K, which is higher than that predicted from the arithmetic, harmonic, and geometric models. The arithmetic model predictions of composite thermal conductivity showed the best agreement with the estimated $k_\theta$. The following factors may contribute to the higher $k_\theta$ values obtained in this work compared to the previously reported estimates and mixing models predictions: (1) the presence of unreacted water in the sample, whereas in all the other measurements the hydrate pore space was filled with gas. Water bridging will occur between liquid water and hydrate particles and thereby help to facilitate heat transfer through the sample. (2) The lack of thermal conductivity data for zero porosity methane hydrate; in the present work, we have shown that the methane hydrate sample formed from granular ice was not homogeneous, and this variation in the sample should be accounted for in the hydrate physical and thermal property measurements. Overall, the present work provides a new technique to estimate the thermal conductivity of a porous methane hydrate sample as a function of density and predicted nonporous methane hydrate thermal conductivity. This work also demonstrates the importance of X-ray computer tomography in hydrate physical and thermal property measurements.

**References and Notes**

(1) Sloan, E. D., Jr. *Clathrate Hydrates of Natural Gases,* 2nd ed.; Marcel Dekker: New York, 1998.

(2) Kvenvolden, K. *Natural Gas Hydrate: Introduction and History of Discovery*; Kluwer Academic Publishers: Dordrecht, The Netherlands, 2000.

(3) Milkov, A. V. *Earth Sci. Rev.* **2004**, *66*, 183.

(4) Durham, W. B.; Kirby, S. H.; Stern, L. A.; Zang, W. *J. Geophys. Res.* **2003**, *108*, 2182.

(5) Waite, W. F.; deMartin, B. J.; Kirby, S. H.; Pinkston, J.; Ruppel, C. D. *Geophys. Res. Lett.* **2002**, *29*, 2229.

(6) Huang, D.; Fan, S. *J. Chem. Eng. Data* **2004**, *49*, 1479.

(7) Cook, J. G.; Leaist, D. G. *Geophys. Res. Lett.* **1983**, *10*(5), 397.

(8) Tse, J. S.; Klein, M. L.; McDonald, I. R. *J. Phys. Chem.* **1983**, *87*, 4198.

(9) Ruppel, C. *Thermal State of the Gas Hydrate Reservoir*; Kluwer Academic Publishers: Dordrecht, The Netherlands, 2000.

(10) Peters, D.; Mehta, A.; Walsh, J. In *Proceedings of the 4th International Conference on Gas Hydrates, Yokohama, Japan, May 19−23, 2002*; Vol. 2, p 952.

(11) Waite, W. F.; Pinkston, J.; Kirby, S. In *Proceedings of the 4th International Conference on Gas Hydrates, Yokohama, Japan, May 19−23, 2002*; p 728.

(12) Huang, D.; Fan, S. *J. Geophys. Res.* **2005**, *110*, B01311, doi: 10.1029/2004JB003314.

(13) Ross, R. G.; Andersson, P.; Backstrom, G. *Nature* **1981**, *290*, 322.

(14) Stern, L. A.; Kirby, S. H.; Circone, S.; Durham, W. B. *Am. Mineral.* **2004**, *89*, 1162.

(15) Moridis, G. J.; Seol, Y.; Kneafsey, T. J. *Fifth International Conference on Gas Hydrates* **2005**, *1004*, 21.

(16) Kneafsey, T. J.; Tomutsa, L.; Moridis, G. J.; Seol, Y.; Freifeld, B. M.; Taylor, C. E.; Gupta, A. *Fifth International Conference on Gas Hydrates* **2005**, *1033*, 213.

(17) Mikami, J.; Masuda, Y.; Uchida, T.; Satoh, T.; Takeda, H. Gas Hydrates, Challenges For The Future. *Ann. NY Acad. Sci.* **2000**, *912*, 1011−1020.

(18) Jin, S.; Takeya, S.; Hayashi, J.; Nagao, J.; Kamath, Y.; Ebinuma, T.; Narita, H. *Jpn. J. Appl. Phys.* **2004**, *43*, 5673.

(19) Freifeld, B. M.; Kneafsey, T. J. In *Advances in the Study of Gas Hydrates*; Taylor, C. E., Kwan, J. T., Eds.; Kluwer Academic Publishers: New York, 2005; p 227.

(20) Freifeld, B. M.; Kneafsey, T. J.; Tomutsa, L.; Stern, L.; Kirby, S. *Proceedings of the 4th International Conference on Gas Hydrates, Yokohama, Japan, May 19−23, 2002*; p 750.

(21) Stern, L. A.; Kirby, S. H.; Durham, W. B. *Science* **1996**, *273*, 1843.

(22) Circone, S.; Kirby, S. H.; Stern, L. A. *J. Phys. Chem. B* **2006**, *110*, 8232.

(23) Dorstewitz, F.; Mewes, D. *Proceedings of the 5th International Offshore and Polar Engineering Conference (ISOPE-5), The Hague, The Netherlands, June 11−16, 1995*; Vol. 1, p 244.

(24) Ballard, A. L.; Sloan, E. D., Jr. *Fluid Phase Equilib.* **2002**, *194−197*, 371.

(25) Abramoff, M. D.; Magelhaes, P. J.; Ram, S. J. *Biophotonics Int.* **2004**, *11*, 36.

(26) Wagner, W.; Pruss, A. *J. Phys. Chem. Ref. Data* **2002**, *31*, 387.

(27) Finsterle, S. *ITOUGH2 User's Guide*, Version 3.1; Report No. LBNL-40041; Lawrence Berkeley National Laboratory: Berkeley, CA, 1999.

(28) Finsterle, S.; Pruess, K. *Water Resource Res.* **1995**, *31*, 913.

(29) Gimmi, T.; Schneebeli, M.; Fluhler, H.; Wydler, H.; Baer, T. *Water Resour. Res.* **1997**, *33*, 589.

(30) Engelhardt, I.; Finsterle, S. *Appl. Clay Sci.* **2003**, *23*, 111.

(31) Finsterle, S.; Faybishenko, B. A. Report No. LBNL-40245; Lawrence Berkeley National Laboratory: Berkeley, CA, 1997.

(32) Friend, D. G.; Ely, J. F. *J. Phys. Chem. Ref. Data* **1989**, *18*, 583.

(33) Kumar, P.; Turner, D.; Sloan, E. D. *J. Geophys. Res.* **2004**, *109*, B01207, doi:10.1029/2003JB002763.

(34) Waite, W. F.; Gilbert, L. Y.; Winters, W. J.; Mason, D. H. *Fifth International Conference on Gas Hydrates* **2005**, *5042*, 1724.

(35) Hirata, A.; Mori, Y. H. *Chem. Eng. Sci.* **1998**, *53*, 2641.